

Active Massive Black Hole Found in the Young Star-Forming Dwarf Galaxy SBS 0335-052E

Shun Hatano^{1,2}, Masami Ouchi^{1,3,2,4}, Kimihiko Nakajima¹, Toshihiro Kawaguchi⁵, Mitsuru Kokubo¹, Satoshi Kikuta¹, Nozomu Tominaga^{1,6,7}, Yi Xu^{3,8}, Kuria Watanabe^{1,2}, Yuichi Harikane³, Yuki Isobe^{3,9}, Akinori Matsumoto^{3,9}, Moka Nishigaki^{1,2}, Yoshiaki Ono³, Masato Onodera¹⁰, Yuma Sugahara^{11,1}, Hiroya Umeda^{3,9}, and Yechi Zhang^{3,9}

¹*National Astronomical Observatory of Japan, Osawa 2-21-1, Mitaka, Tokyo 181-8588, Japan*

²*Department of Astronomical Science, The Graduate University for Advanced Studies, SOKENDAI, 2-21-1 Osawa, Mitaka, Tokyo, 181-8588, Japan*

³*Institute for Cosmic Ray Research, The University of Tokyo, 5-1-5 Kashiwanoha, Kashiwa, Chiba 277-8582, Japan*

⁴*Kavli Institute for the Physics and Mathematics of the Universe (WPI), University of Tokyo, Kashiwa, Chiba 277-8583, Japan*

⁵*Department of Economics, Management and Information Science, Onomichi City University, Hisayamada 1600-2, Onomichi, Hiroshima 722-8506, Japan*

⁶*Astronomical Science Program, Graduate Institute for Advanced Studies, SOKENDAI, 2-21-1 Osawa, Mitaka, Tokyo 181-8588, Japan*

⁷*Department of Physics, Faculty of Science and Engineering, Konan University, 8-9-1 Okamoto, Kobe, Hyogo 658-8501, Japan*

⁸*Department of Astronomy, Graduate School of Science, the University of Tokyo, 7-3-1 Hongo, Bunkyo, Tokyo 113-0033, Japan*

⁹*Department of Physics, Graduate School of Science, The University of Tokyo, 7-3-1 Hongo, Bunkyo, Tokyo 113-0033, Japan*

¹⁰*Subaru Telescope, National Astronomical Observatory of Japan, National Institutes of Natural Sciences (NINS), 650 North A'ohoku Place, Hilo, HI 96720, USA*

¹¹*Waseda Research Institute for Science and Engineering, Faculty of Science and Engineering, Waseda University, 3-4-1 Okubo, Shinjuku, Tokyo 169-8555, Japan*

Since the late 20th century, young star-forming dwarf galaxies with extremely low heavy-element abundances have been identified in the local universe¹⁻³. Such a population of galaxies, represented by SBS 0335-052E, is intensively studied as a laboratory of galaxy formation, and interpreted as galaxies with hard emission and energetic outflows driven by massive stars^{2,4,5}. Here we report the temporal flux variability of SBS 0335-052E in $3 - 4 \mu\text{m}$ bands on timescale of months to years with dimming and brightening up to 50% over 12 years. This is a clear signature of dust torus emission of an active massive black hole in SBS 0335-052E. The deep optical spectrum reveals a very broad component with $1.24 (\pm 0.01) \times 10^4 \text{ km s}^{-1}$ in $\text{H}\alpha$ emission, suggesting emission originated from broad line regions around the massive black hole. The black hole mass is estimated to be ~ 100 thousand solar masses from the spectral energy distribution. This is the first example of the massive black hole existence in a long-considered young star-forming dwarf galaxy.

SBS 0335-052E is known to be a star-forming dwarf galaxy with a low stellar mass of $M_* \lesssim 10^7 M_\odot$ (ref.^{6,7}). Because it has extremely low heavy-element abundance of $\sim 1/40 Z_\odot$ (ref.⁸), SBS 0335-052E has been studied as a laboratory of young star-forming galaxy over the

past 30 years². The near-infrared observations with the *Hubble Space Telescope (HST)* identify the hot (~ 800 K) dust continua that could be made by the extreme star-forming activity in dense and dusty star-forming regions^{7,9}, while the colors in the near-infrared bands (*W1* and *W2* bands) fall in the regime of active galactic nucleus (AGN) with hot dust emission¹⁰. The optical spectrum of SBS 0335-052E shows [Ne v] and [Fe v] emission lines, often found in metal-poor star-forming galaxies, requiring high-energy ionizing emission that are thought to originate from (a) hard ionizing source(s)⁵ that may be an extreme stellar population, fast-radiative shock, X-ray binaries, or AGN. The origins of the NIR colors and the high-ionizing emission lines found in SBS 0335-052E are unclear.

Here, we investigate variabilities of the near-infrared (NIR) emission that are key to understanding the physical origin. We use the NIR multi-epoch imaging data of the Wide-field Infrared Survey Explorer (*WISE*) mission consisting of the AllWISE and NEOWISE data sets that monitor SBS 0335-052E at the epoch ranging in 2010-2022. We obtain *W1* ($3.4 \mu\text{m}$) and *W2* ($4.6 \mu\text{m}$) band photometry for 18 epochs available via the Infrared Processing and Analysis Center (IPAC) Infrared Science Archive (see Methods). Figure 1 presents the light curves in *W1* and *W2* bands for SBS 0335-052E. To distinguish between real variabilities and systematic offsets of the photometry over the epochs, we evaluate the systematic offsets with NIR sources having similar magnitudes around the position of SBS 0335-052E. We find that the systematic offsets are small, within 0.03 mag (0.05 mag) for the *W1* (*W2*) band, over the epoch that are presented in Figure 1 (see Methods). Figure 1 indicates that the light curves of SBS 0335-052E show clear time variabilities both in the *W1* and *W2* band images that are significantly brightened by 0.4 and 0.2 magnitudes cor-

responding to the luminosity variabilities by $\sim 50\%$ and 20% from modified Julian date (MJD) ~ 57000 to 59000 at the $\gtrsim 20$ and 6σ significance levels for the $W2$ and $W1$ bands, respectively. These significant time variabilities are confirmed on the individual *WISE* images (Top panels in Figure 1, see also Methods). Moreover, there is a significant dimming in the $W2$ band from MJD 55600 to 56800 at the $\sim 7\sigma$ level. We also find higher frequency variations at the $2-3\sigma$ levels at the epoch around MJD 58900 in the $W2$ band.

The month-to-year scale variabilities of the NIR light curves indicate that the emission originates from a compact object. There are two possibilities for the origin of the observed NIR flux variations: dust emission associated with a supernova explosion and dust torus emission from an active massive black hole. Although a simple brightening in the $W1$ and $W2$ bands at MJD $\sim 57000-59000$ might be explained by either of the possible origins, the ~ 1000 -day-long dimming such found at MJD $55600-56800$ is not observed in typical supernovae^{11,12}. While there are difficulties in explaining the observed light curves by a supernova explosion, all of these variations are naturally explained by a massive black hole with flux variabilities of the dust torus NIR emission driven by stochastic ultraviolet(UV)-optical flux variabilities of the accretion disk emission.¹³⁻¹⁵

In Figure 1, the amplitudes of the $W2$ variabilities are significantly larger than those of the $W1$ variabilities suggesting that the NIR emission is strongly reddened by dust (see Methods). The visual extinction from the $W1$ and $W2$ variabilities is estimated to be high, $A_V = 107 \pm 12$ mag, corresponding to lower limit of $\log(N_H/\text{cm}^{-2}) = 23.2$ in hydrogen column density (see Methods). The large hydrogen column density suggests that the massive black hole of SBS 0335-

052E is heavily-obscured.

We conducted optical spectroscopy for SBS 0335-052E with the Low Resolution Imaging Spectrometer (LRIS) spectrograph on the 10m Keck I telescope (Keck/LRIS). The $H\alpha$ emission line consists of three components, narrow, medium, and broad components whose full widths at half maximum (FWHMs) are $1.58 (\pm 0.001) \times 10^2$, $1.29 (\pm 0.01) \times 10^3$, and $1.24 (\pm 0.01) \times 10^4$ km s^{-1} , respectively (Figure 2, see also Methods)¹. The velocity width of the broad component is very large ($\gtrsim 10^4$ km s^{-1}). Such a large velocity width can be explained by emission from the broad line region (BLR) around the massive black hole. Since SBS 0335-052E is likely a heavily-obscured active massive black hole, the broad component may be the emission from the BLR reflected by the electron surrounding the black hole. Assuming that the broad line component originates from the BLR, we calculate the black hole mass to be $M_{\text{BH}} = 1.1 (\pm 0.3) \times 10^7 M_{\odot}$ with the $H\alpha$ broad line width and luminosity $L_{H\alpha} = 1.81 (\pm 0.02) \times 10^{39}$ erg s^{-1} by the estimation method of black hole masses established for Type 1 AGNs¹⁶. If the reflection produces the broad line emission, the upper limit of the black hole mass is placed at $M_{\text{BH}} \lesssim 1.4 (\pm 0.3) \times 10^8 M_{\odot}$ (see Methods).

Figure 3 shows the spectral energy distribution (SED) of SBS 0335-052E. We compare the SED with CIGALE v2022.1 (ref. ¹⁷) models in the optical to sub-millimeter bands, and obtain the best-fit SED model shown in Figure 3 (see Methods). The best-fit model is composed of young stellar and obscured AGN components (see Methods). The NIR to mid-infrared emission of SBS 0335-052E is naturally explained by the dust torus emission of the obscured AGN. The intrinsic

¹Such broad components appeared in the VLT spectrum taken in 2003 (Figure 5 of ref.⁵), indicating that the broad line exists for more than 10 years.

AGN bolometric luminosity is estimated to be $L_{\text{bol}} = 1.21 \times 10^{43} \text{ erg s}^{-1}$ with the best-fit SED by the CIGALE modeling. The relation between the Eddington luminosity (L_{Edd}) and the black hole mass M_{BH} is given by

$$L_{\text{Edd}} = 1.2 \times 10^{38} \left(\frac{M_{\text{BH}}}{M_{\odot}} \right) \text{ erg s}^{-1}. \quad (1)$$

The estimated intrinsic AGN bolometric luminosity corresponds to the L_{Edd} of a black hole with a mass of $1.0 \times 10^5 M_{\odot}$. Because the dust torus NIR emission is typically observed in AGNs with Eddington ratios of $L_{\text{bol}}/L_{\text{Edd}} \sim 0.01 - 10$ (ref. ¹⁸⁻²⁰), the black hole mass of SBS 0335-052E should range in $\sim 10^4 - 10^7 M_{\odot}$. We compute the expected X-ray emission of the AGN from the best-fit model, and apply photoelectric absorption and Thomson scattering effects with the lower limits of the hydrogen column densities of $\log(N_{\text{H}}/\text{cm}^{-2}) \geq 23.2$ and 24.8 (see Methods). We present the expected AGN X-ray emission model in Figure 3, and find that there is a possibility that the expected AGN X-ray emission is much lower than the observed Chandra X-ray emission. Moreover, our lower limits of the absorption are not consistent with the absorption indicated from the X-ray data, $\log(N_{\text{H}}/\text{cm}^{-2}) \sim 21.8$ (ref.⁴). These discrepancies are not real, if the observed X-ray emission is not originated from the AGN but from the galaxy X-ray emission composed of low/high mass X-ray binaries and hot gas. We find that the observed X-ray emission is reproduced by the galaxy X-ray emission model (Figure 3, see also Methods). The scenario of the galaxy X-ray emission agrees with the spatially extended X-ray emission hinted by ref^{4,21}.

The SBS 0335-052E is an unique galaxy among dwarf galaxies with massive black holes. Figure 4 compares SBS 0335-052E with such dwarf galaxies on the black hole vs. stellar mass plane. SBS 0335-052E is significantly less massive than those of the dwarf galaxies by 1 – 2 orders

of magnitude in stellar mass.^{22–24} In Figure 4, we also compare SBS 0335-052E with high- z ($z \gtrsim 4$) star-forming galaxies with weak broad lines recently identified by *James Webb Space Telescope* observations^{25–27}. While SBS 0335-052E may be a local counterpart of the star-forming galaxies at $z \gtrsim 4$ with weak broad lines, we find that the stellar mass of SBS 0335-052E is significantly less massive than the seven of the high- z star-forming galaxies with a stellar mass determination of $M_* \sim 10^9 - 10^{10} M_\odot$. While the upper limits of the stellar masses are only given for the four of the high- z galaxies, these four galaxies have metallicities ($0.2 - 0.4 Z_\odot$) significantly larger than SBS 0335-052E by one order of magnitude^{26,27}. There are no dwarf galaxies with massive black holes whose properties are equivalent to those of SBS 0335-052E known to date.

The high resolution NIR continuum image of SBS 0335-052E taken with *HST* resolves the *WISE* source into NIR sources including two major components with hot dust dubbed SSC1 and SSC2 that are close with a distance of ~ 100 pc on the sky⁷. Because the broad $H\alpha$ line is found at the position including SSC1 and SSC2 (see Methods), the *WISE* variability of NIR emission should originate from SSC1 and SSC2. SSC1 and SSC2 have similar stellar masses and ages ($M_* \sim 1 \times 10^6 M_\odot$ and $\lesssim 3$ Myr) and exhibit emission from hot dust with ~ 800 K (ref.⁷). Although the hot dust may be heated by extreme star formation in principle, the high temperature may suggest that each of SSC1 and SSC2 harbors a massive black hole as the dust heating source. Because SSC1 and SSC2 are close sources with a distance of only ~ 100 pc, the massive black hole of SBS 0335-052E is potentially a candidate of dual massive black holes on the way towards a merger event.

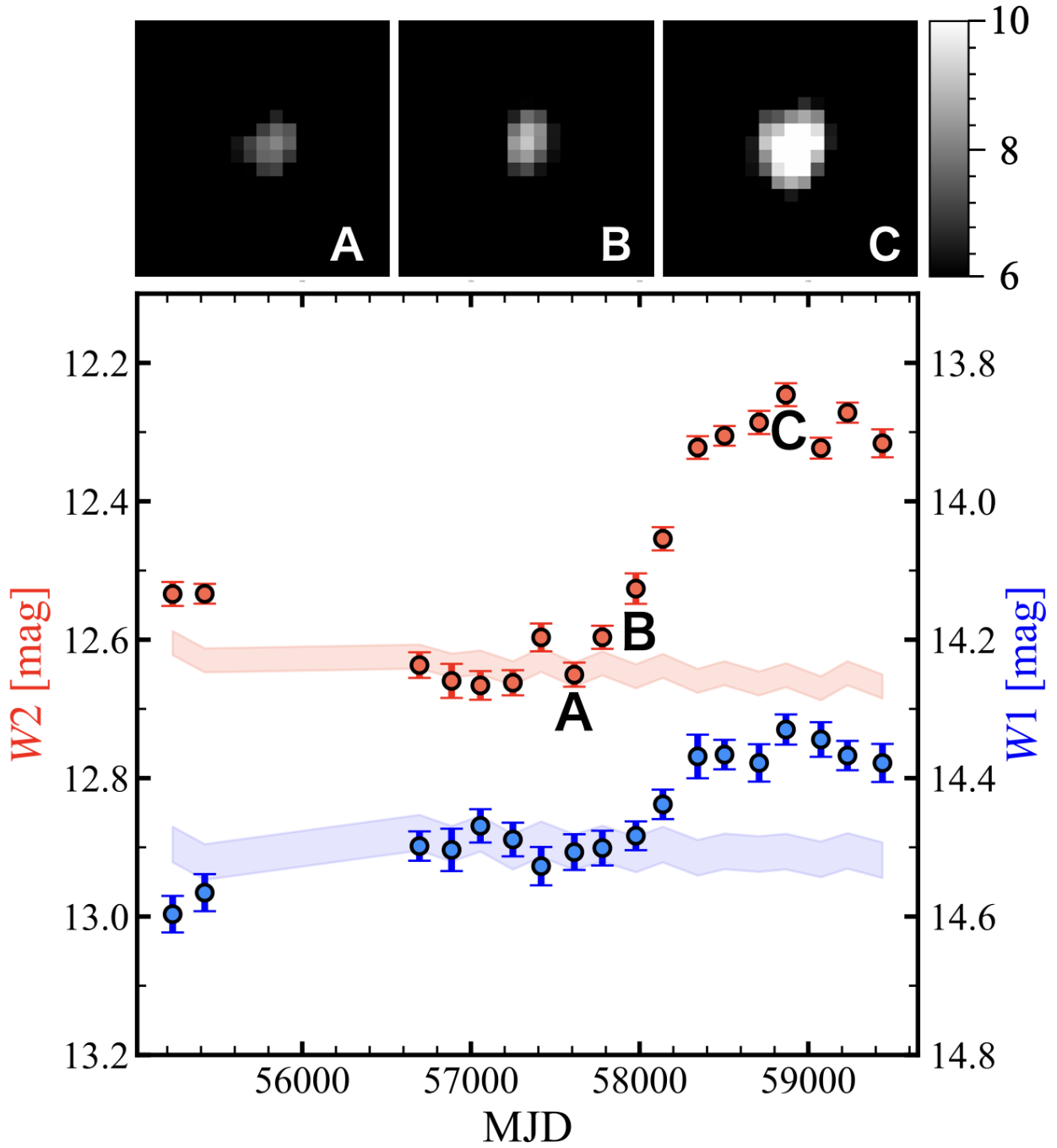


Figure 1 | Near-infrared time variabilities of SBS 0335-052E. The red and blue circles indicate the $W2$ and $W1$ band magnitudes, respectively. The three images on the top of the figure show the $W2$ band snapshots of SBS 0335-052E taken in MJD 57613, 57977, and 58868. The red (blue) shaded curve denotes

the systematic offset of $W2$ ($W1$) band magnitudes normalized at MJD 57613. The widths of the shaded regions indicate photometric errors of $W1$ and $W2$ bands of SBS 0335-052E in MJD 57613. The errors of systematic offsets are much smaller than the photometric errors. The color bar of the Top panels represents the number count of each pixel of the *WISE* $W2$ band image.

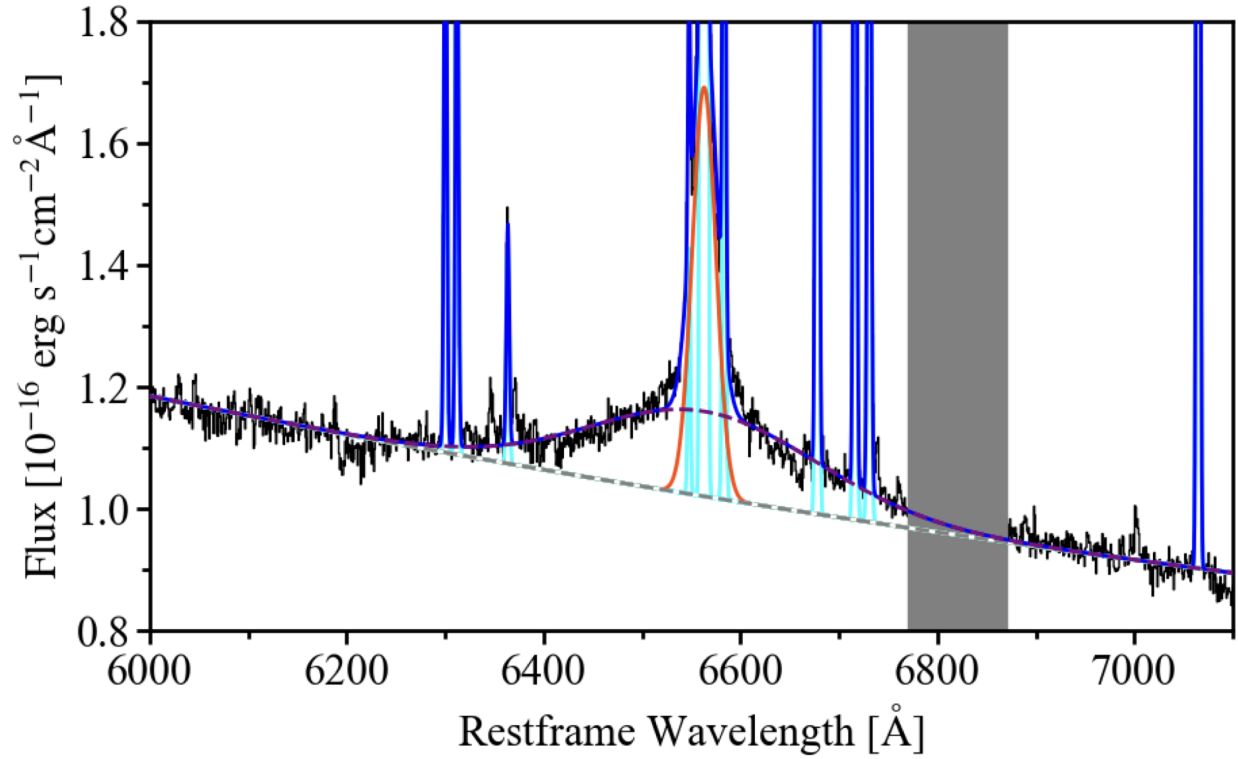


Figure 2 | Optical spectrum of SBS 0335-052E (black line). The solid cyan, solid orange, and dashed purple curves represent the best-fit emission lines of the narrow, medium, and broad components, respectively. The blue curve denotes the total fluxes of the best-fit emission lines. The grey shade indicates the spectrum contaminated by night sky emissions, which are masked out in our emission-line model fitting (see Methods). The dashed grey line represents the best-fit continuum emission.

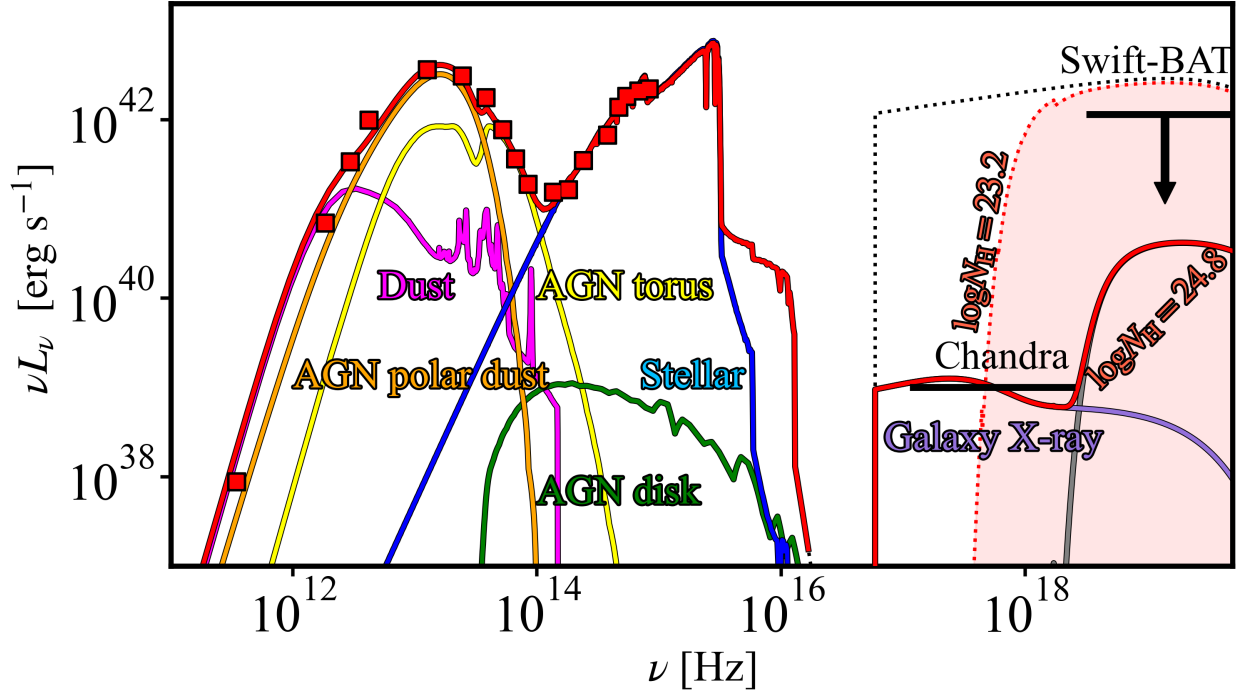


Figure 3 | SED of SBS 0335-052E. The red squares and the black bars indicate the measurements of SBS 0335-052E. The red line at $\lesssim 10^{16}$ Hz represents the best-fit SED. The dust over the galaxy, AGN torus, AGN polar dust, AGN disk, and stellar components of the best-fit SED are shown with the magenta, yellow, orange, green, and blue curves, respectively. The dotted black line denotes the intrinsic X-ray spectra calculated from the best-fit SED. The red dotted and grey solid lines present the net transmitted X-ray spectra calculated from the intrinsic X-ray spectra with the hydrogen column density of $\log(N_{\text{H}}/\text{cm}^{-2}) = 23.2$ and 24.8, respectively. The red shade indicates the range of the net transmitted X-ray spectra allowed for SBS 0335-052E. The purple curve indicates the model of the galaxy X-ray emission. The red solid curve at $\gtrsim 10^{16}$ Hz represents the the sum of the galaxy X-ray emission and the transmitted X-ray emission for the hydrogen column density of $\log(N_{\text{H}}/\text{cm}^{-2}) = 24.8$.

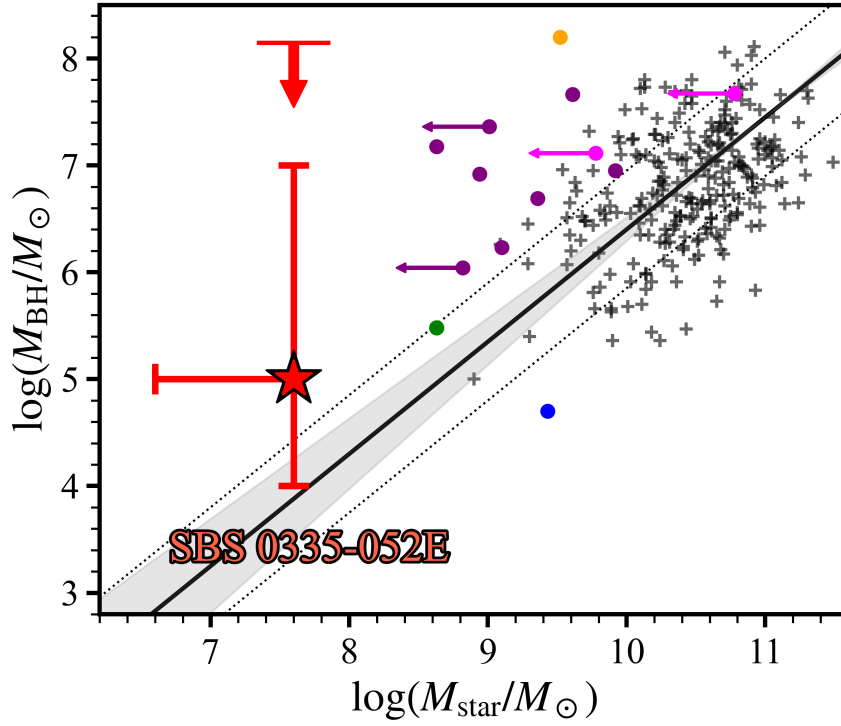


Figure 4 | Stellar mass to black hole mass relation. The red star mark represents the black hole (stellar) mass of SBS 0335-052E calculated by the SED fitting (taken from the literature^{6,7}). The downward arrow indicates the upper limit of the black hole mass derived from the spectral fitting for the emission line. The black crosses are black hole and stellar masses of local dwarf galaxies with massive black holes taken from ref.²². The blue (green) circle is a local low-mass AGN taken from ref.²³ (ref.^{22,24}). The magenta, orange, and purple circles denote high redshift galaxies recently identified by ref.²⁶, ref.²⁵, and ref.²⁷, respectively, where we omit two objects of ref.²⁶ from the data points of ref.²⁷. The black solid line and the grey shade show the best-fit line and 1σ error of the local relation in the range of $M_{\text{BH}} = 10^5 - 10^{8.5} M_{\odot}$ provided by ref.²². The dotted lines present the sum of intrinsic scatter and measurement uncertainty in the local relation.

Acknowledgements We thank K. Shimasaku, T. Tanaka, S. Huang, and R. Kawabe for useful discussion. This research is based in part on data gathered with the 10-meter Keck Telescope located at W. M. Keck Observatory. We thank the observatory personnel for help with the observations. This work was supported by the joint research program of the Institute of Cosmic Ray Research (ICRR), the University of Tokyo. This work was supported by the World Premier International Research Center Initiative (WPI Initiative), MEXT, Japan, as well as KAKENHI Grant-in-Aid for Scientific Research (19H00697, 20H00180, 21H04467, and 21K03622) through the Japan Society for the Promotion of Science (JSPS).

Author Contributions SH identified the variabilities of SBS 0335-052E in the NEOWISE data base. MK evaluated the systematics of the variabilities, and confirmed the variabilities in the NEOWISE data. KN, MO, SH, and KW carried out the Keck/LRIS observations. SH conducted the Keck/LRIS data reduction and analysis with assistance of KN and YX, and obtained the best-fit SED and physical parameters. SH, MO, and MK developed the main interpretation of the results. SH and MO wrote the main text and the Methods section. All authors discussed the results and commented on the manuscript.

Author Information The authors declare no competing interests. The datasets generated during and/or analysed during the current study are available from the corresponding author on reasonable request. Correspondence and requests for materials should be addressed to SH. (shun.hatano@grad.nao.ac.jp). Reprints and permissions information is available at www.nature.com/reprints.

Methods

Cosmology The cosmological parameters adopted in this paper are $H_0 = 73 \text{ km s}^{-1} \text{ Mpc}^{-1}$, $\Omega_m = 0.24$, and $\Omega_\Lambda = 0.76$, determined by Planck observations²⁸.

Multi-epoch near-infrared photometry We use multi-epoch $W1$ ($3.4 \mu\text{m}$) and $W2$ ($4.6 \mu\text{m}$) band NIR photometric data taken by the *WISE* mission to explore the time variability in SBS 0335-052E. *WISE* has acquired all-sky NIR and mid-infrared images including the $W1$ and $W2$ band data by 2010 (ref.²⁹) by the mission dubbed AllWISE, and extended the mission dubbed NEOWISE in the post-cryophase for the $W1$ and $W2$ band data twice a year on average since 2013 (ref.³⁰). The time baseline of the $W1$ and $W2$ band data released so far spans 11 years (NEOWISE 2022 Data Release). We retrieve multi-epoch $W1$ and $W2$ band photometry of SBS 0335-052E from the WISE All-Sky and NEOWISE Single Exposure (L1b) Source Tables available at IRSA using a cone search radius of 2 arcsec. The photometric data of SBS 0335-052E were obtained in 18 visits, 2 of which were covered by AllWISE in 2010 and the remaining 16 by NEOWISE in 2014-2021. Each visit consists of $\gtrsim 10$ frames taken in several days. We calculate a weighted mean and standard error of the multiple magnitude measurements in each visit, removing erroneous measurements with standard photometry flags². We obtain a total of 18 photometric measurements and errors for each band in the epoch of 2010-2021. The light curves of the $W1$ and $W2$ bands are shown in Figure 1. The *WISE* magnitudes given in the Vega magnitude system are converted into fluxes with zero-point fluxes of $f_{\nu,0} = 309.540$ and 171.787 Jy for the $W1$ and $W2$ bands, respectively.

²https://wise2.ipac.caltech.edu/docs/release/neowise/expsup/sec2_3.html

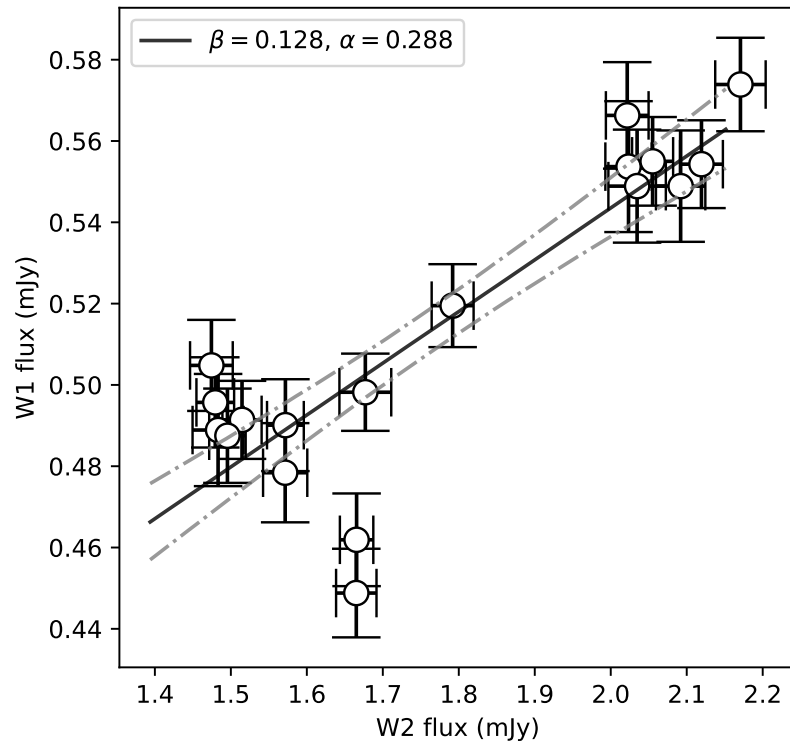
The $W1$ and $W2$ photometry may include systematic offsets due to time-dependent and position-dependent flux zero-point determination.³¹ We evaluate the systematic offsets of *WISE* $W1$ and $W2$ photometry with AllWISE sources having the non-variable flags that reside within 3600 arcsec from SBS 0335-052E. There are 1312 (270) AllWISE sources with NIR band magnitudes of $W1 = 14.517 \pm 0.5$ mag ($W2 = 12.528 \pm 0.5$ mag) comparable with those of SBS 0335-052E. We cross match the AllWISE sources with the NEOWISE single-epoch photometry table (L1b), and create a light curve for each object. We average the light curves normalized with $W1$ and $W2$ magnitude taken from AllWISE Source Catalog, and obtain the systematic offsets. The $W1$ and $W2$ light curves corrected for the systematic offsets are shown in Extended Data Figure 2.

We create coadd images of the $W1$ and $W2$ band of SBS 0335-052E for each epoch with an online version of the WISE/NEOWISE Coadder ICORE^{32,33} with default parameters.

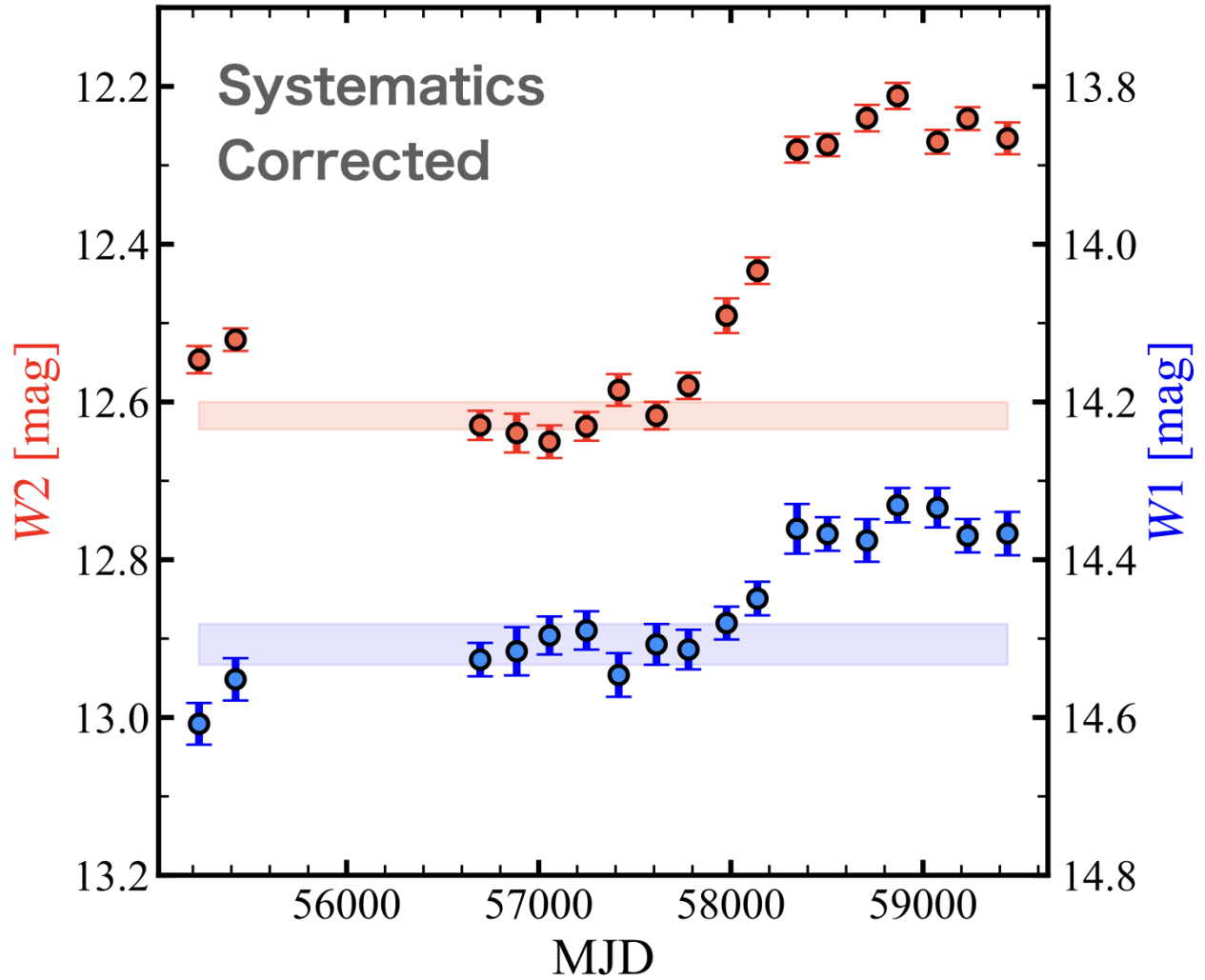
NIR properties of the variable component Extended Data Figure 1 shows *WISE* $W1$ and $W2$ fluxes for all of the observing epochs. There is a positive correlation between the $W1$ and $W2$ fluxes that ranges in 0.4488–0.5739 and 1.4744–2.1707 mJy, respectively. Over this observing epoch, $W1$ and $W2$ fluxes increase by $\Delta f_{W1} = 0.1251$ ($= 0.5739 - 0.4488$) and $\Delta f_{W2} = 0.6963$ ($= 2.1707 - 1.4744$) mJy, respectively, from the faintest observed fluxes. We conduct blackbody-function fitting to the two data points of Δf_{W1} and Δf_{W2} with two free parameters of the blackbody temperature and intensity. The best-fit blackbody temperature of the variable component (hereafter $W1 - W2$ color temperature) is 419 ± 23 K.

Unobscured AGNs with dust torus exhibit high $W1 - W2$ color temperatures of $\sim 1,000$ K that are close to the dust sublimation temperature³⁴, which implies that the NIR variability of AGNs originate from the innermost region of the dust torus. Contrary to the high $W1 - W2$ color temperatures of the unobscured AGNs, the $W1 - W2$ color temperature of SBS 0335-052E which shows the massive black hole signatures in the NIR bands is low (419 ± 23 K). This suggests that the amount of reddening of the NIR variable emission of SBS 0335-052E is large, which can be attributed to the dust extinction of the outer dusty torus. Following ref.³⁴, the $W1 - W2$ color of the variable component in SBS 0335-052E, represented by flux variation gradient $\Delta W1/\Delta W2$, is evaluated by fitting a linear regression line ($y = \alpha + \beta \times x$) to the flux-flux plot of the $W1$ and $W2$ band light curves (Extended Data Figure 1). From the linear regression analysis with the Josh Meyers' Python port of `linmix_err`³⁵, we obtain $\beta = \Delta W1/\Delta W2 = 0.128 \pm 0.022$ (Extended Data Figure 1). By comparing with the typical value for unobscured AGNs of $\beta = 0.86 \pm 0.10$ (ref. ³⁴), we get a color excess between the $W1$ and $W2$ bands of SBS 0335-052E as $E(W1 - W2) = A_{W1} - A_{W2} = 2.067 \pm 0.186$ mag. This color excess corresponds to a visual extinction of $A_V = 107 \pm 12$ mag, assuming Fitzpatrick's dust extinction curve³⁶. The high visual extinction indicates the massive black hole of SBS 0335-052E is viewed nearly edge-on³⁷, which is consistent with the result of the SED fitting (Extended Data Table 3). Assuming a metallicity-dependent gas-to-dust ratio of $N_H/A_V = 10^{21.25-21.43}(Z/Z_\odot)^{-1}\text{cm}^{-2}\text{mag}^{-1}$ (ref.³⁴), we obtain hydrogen column densities as $\log(N_H/\text{cm}^{-2}) = 23.2$ and 24.8 for $Z = Z_\odot$ and $Z = Z_\odot/40$, respectively. We note that the estimated hydrogen column densities are lower limits of the actual hydrogen gas column densities because a large fraction of the N_H measured in X-ray-obscured

AGNs is supposed to be contributed from dust-free gas particles inside the dust sublimation radius of the dust torus, namely the BLR³⁴. The large hydrogen column density implies that SBS 0335-052E is a heavily obscured or Compton-thick massive black hole.



Extended Data Figure 1 | *WISE* W2 and W1 fluxes of SBS 0335-052E (Circles). The solid line is the best-fit linear regression line, and the dot-dashed lines indicate the 16 – 84% percentile range.



Extended Data Figure 2 | *WISE* *W2* and *W1* magnitudes corrected with systematic offsets.

Keck/LRIS spectroscopy and data reduction. We carried out spectroscopic observations for SBS 0335-052E under the photometric condition on 8th of November, 2021 (MJD: 59526;PI: K.Nakajima). We used the 600/4000 grism and 600/7500 grating in the blue and red channels, respectively. A spectral resolution of the blue (red) channel was $\sim 4(5)$ Å in FWHM. The slit width and length were 0.7 arcsec and 90 arcsec, respectively. The position and the position angle

were the same as those chosen by ref.⁵ who targeted an unresolved (~ 0.3 arcsec; ref.⁷) luminosity peak made of SSC1 and SSC2 in SBS 0335-052E. The seeing sizes ranged in $0.8 - 1.0$ arcsec. The exposure time of blue (red) channel was 3600 (3360) seconds. We also observed a standard star Feige 34 for a flux calibration. The data reduction is conducted in the same manner as ref.³⁸ using the IRAF package. We obtain one-dimensional spectra of SBS 0335-052E, summing up two-dimensional spectra along the spatial axis with a width of 1.6 arcsecond corresponding to a FWHM of the $H\alpha$ emission line. We correct fluxes for a slit loss that is estimated with the spatial profile of the $H\alpha$ emission along the slit.

Spectral fitting We determine a line spread function (LSF) for the red channel of the LRIS instrument with the strong night skyline found in the science frames. We perform line profile fitting with `scipy.optimize` package³⁹ to the $H\alpha$, $[N\ II]\lambda 6548, 6583$, $[O\ I]\lambda 6364$ line and the other 6 weak emission lines using the LSF with free parameters of line fluxes, widths, and central wavelengths, fitting the continuum emission using power-law with free parameters of a power-law index and an amplitude. The faint emission lines weaker than the $[O\ I]\lambda 6364$ line and the strong night skylines that could contaminate the spectra are masked while the line profile fitting. We find that there is a significant line broadening in the $H\alpha$ line of SBS 0335-052E. Although we include one additional line component for the $H\alpha$ -line fitting, there remains a very broad component. We thus include one more component, and conduct the line profile fitting with three components dubbed narrow, medium, and broad components that well explain the observed $H\alpha$ line (Figure 2). We find that the line widths of the narrow, medium and broad components are $1.58 (\pm 0.001) \times 10^2$, $1.29 (\pm 0.01) \times 10^3$, and $1.24 (\pm 0.01) \times 10^4$ km s⁻¹, respectively, in the best-fit profiles. The

best-fit parameters are summarised in Extended Data Table 2. The luminosity of the broad H α emission $L_{\text{H}\alpha}$ is $L_{\text{H}\alpha} = 1.81 (\pm 0.02) \times 10^{39} \text{ erg s}^{-1}$.

Black hole mass estimate with a broad component SBS 0335-052E exhibits a broad component in H α line with an FWHM of $\sim 10^{3-4} \text{ km s}^{-1}$. The virial mass of a massive black hole is estimated with the relationship calibrated with masses measured by reverberation mapping¹⁶:

$$M_{\text{BH}} = 2.0_{-0.3}^{+0.4} \times 10^6 M_{\odot} \left(\frac{L_{\text{H}\alpha}}{10^{42} \text{ erg s}^{-1}} \right)^{0.55 \pm 0.02} \left(\frac{\text{FWHM}_{\text{H}\alpha}}{1000 \text{ km s}^{-1}} \right)^{2.06 \pm 0.06}, \quad (2)$$

where $L_{\text{H}\alpha}$ and $\text{FWHM}_{\text{H}\alpha}$ are the intrinsic luminosity and the FWHM of broad H α emission, respectively. With $L_{\text{H}\alpha}$ and $\text{FWHM}_{\text{H}\alpha}$ of the SBS 0335-052E obtained in our observations (Extended Data Table 2), we obtain the black hole mass of $M_{\text{BH}} = 1.1 (\pm 0.3) \times 10^7 M_{\odot}$. Because the broad H α line of SBS 0335-052E is likely to be a scattered emission by the dense gas around the massive black hole, the intrinsic H α line may be brighter than the observed broad H α luminosity. The scattering efficiencies ϵ of AGNs with the detection of scattered H α broad lines are typically $\epsilon \gtrsim 0.01$. We assume the lower limit of the ϵ of SBS 0335-052E is 0.01 and derive the upper limit of the H α intrinsic luminosity as $L_{\text{H}\alpha} \lesssim 1.81 (\pm 0.02) \times 10^{41} \text{ erg s}^{-1}$. Because the scattering may broaden the H α line, the observed H α width may be broader than the intrinsic broad line originated from the broad line region of the black hole (thermal broadening and/or Raman scattering of UV photons by hydrogen atoms). Given the upper limit of the broad H α luminosity and FWHM, we give an upper limit to the black hole mass as $M_{\text{BH}} \lesssim 1.4 (\pm 0.3) \times 10^8 M_{\odot}$. If the medium component originates from a black hole, the black hole mass associated with the medium component is calculated as $M_{\text{BH}} = 7.1 (\pm 1.6) \times 10^4 M_{\odot}$ with $L_{\text{H}\alpha} = 9.04 (\pm 0.08) \times 10^{38} \text{ erg s}^{-1}$.

SED of SBS 0335-052E Figure 3 presents the SED of SBS 0335-052E. We take the photometric measurements of SBS 0335-052E from the literature in the optical to sub-millimeter bands⁴⁰. In the hard X-ray band, we use the data of the 105-Month *Swift*-BAT All-sky Hard X-Ray Survey⁴¹, and identify no detections in SBS 0335-052E. We place an upper limit of $< 8.40 \times 10^{-12} \text{ erg s}^{-1} \text{ cm}^{-2}$ at the 14–195 keV band.⁴¹ In the soft X-ray band, the Chandra data show X-ray emission of $(2.8 - 3.5) \times 10^{39} \text{ erg s}^{-1}$ at 0.5–10.0 keV (ref.⁴).

We fit the SEDs of the CIGALE models to the one of SBS 0335-052E, and determine the best-fit model. Because the CIGALE fitting code needs absorption-corrected X-ray fluxes that are not obtained by observations¹⁷, the model fitting is conducted in the optical to sub-millimeter bands. We summarize the modules and parameter ranges used in the SED fitting in Extended Data Table 3, and present the best-fit model in Figure 3. The best-fit SED explains the overall shape of the SBS 0335-052E SED, being dominated by the cold dust at $\sim 10^{12-13} \text{ Hz}$, the AGN polar dust at $\sim 10^{13-14} \text{ Hz}$, and stars at $\sim 10^{14-15.5} \text{ Hz}$ with a negligible contribution of AGN disk. The black dotted curve in Figure 3 indicates the intrinsic X-ray emission predicted from the best-fit model with $\alpha_{\text{ox}} = -1.1$, $\delta_{\text{LMXB}} = -1.3$, and $\delta_{\text{HMXB}} = -1.3$, where α_{ox} , and δ_{LMXB} (δ_{HMXB}) are the optical to X-ray spectral index and the deviation from the expected X-ray luminosity of low mass X-ray binary (high mass X-ray binary) defined in ref.⁴², respectively. The value of α_{ox} is chosen with the AGN intrinsic luminosity per frequency at 2500 Å of the best-fit SED, $L_{2500\text{\AA}}^{\circ}$, and the $\alpha_{\text{ox}}-L_{2500\text{\AA}}^{\circ}$ relation given by ref.⁴³ To compare the intrinsic X-ray emission given by the model, we apply photoelectric absorption and Thomson scattering effects to the intrinsic X-ray emission with the photoelectric-absorption cross sections (Table 2 of ref.⁴⁴) and the Thomson scattering

cross section, assuming two hydrogen column densities of $\log(N_{\text{H}}/\text{cm}^{-2}) = 23.2$ and 24.8 that correspond to the values obtained from the NIR variability in the solar and $1/40$ solar metallicities, respectively.

References

1. Searle, L. & Sargent, W. L. W. Inferences from the Composition of Two Dwarf Blue Galaxies. *Astrophys. J.* **173**, 25 (1972).
2. Izotov, I. I., Guseva, N. G., Lipovetskii, V. A., Kniazev, A. I. & Stepanian, J. A. Unusually low heavy-element abundance found in the blue compact dwarf galaxy SBS0335-052. *Nature* **343**, 238–240 (1990).
3. Nakajima, K. et al. EMPRESS. V. Metallicity Diagnostics of Galaxies over $12 + \log(\text{O}/\text{H}) \simeq 6.9\text{--}8.9$ Established by a Local Galaxy Census: Preparing for JWST Spectroscopy. *Astrophys. J. Suppl. Ser.* **262**, 3 (2022). 2206.02824.
4. Thuan, T. X., Bauer, F. E., Papaderos, P. & Izotov, Y. I. Chandra Observations of the Three Most Metal Deficient Blue Compact Dwarf Galaxies Known in the Local Universe, SBS 0335-052, SBS 0335-052W, and I Zw 18. *Astrophys. J.* **606**, 213–220 (2004). astro-ph/0401349.
5. Izotov, Y. I., Guseva, N. G., Fricke, K. J. & Papaderos, P. SBS 0335-052E+W: deep VLT/FORS+UVES spectroscopy of the pair of the lowest-metallicity blue compact dwarf galaxies. *Astron. Astrophys.* **503**, 61–72 (2009). 0907.2116.
6. Pustilnik, S. A., Pramskij, A. G. & Kniazev, A. Y. SBS 0335-052 E and W: Implications of new broad-band and $\text{H}\alpha$ photometry. *Astron. Astrophys.* **425**, 51–65 (2004). astro-ph/0405610.

SBS 0335-052E		
wavelength [μm]	flux [mJy]	Reference
0.360	0.73 ± 0.021	(1), (5)
0.440	0.73 ± 0.013	(1), (5)
0.550	0.85 ± 0.015	(1), (5)
0.641	0.81 ± 0.007	(1), (5)
0.791	0.49 ± 0.004	(1), (5)
1.25	0.40 ± 0.023	(2), (5)
1.65	0.25 ± 0.0493	(2), (5)
2.20	0.31 ± 0.1320	(2), (5)
3.55	0.62 ± 0.3890	(3), (5)
4.49	1.50 ± 0.0493	(3), (5)
5.73	4.07 ± 0.1320	(3), (5)
7.87	12.73 ± 0.3890	(3), (5)
12.3	35 ± 6	(4), (5)
23.7	79.0 ± 3.12	(3), (5)
71.1	64.4 ± 5.7	(5)
101.2	31.3 ± 4.75	(5)
162.7	10.4 ± 3.5	(5)
866.5	0.07 ± 0.070	(5)
band [keV]	luminosity [erg s^{-1}]	Reference
0.5–10.0	3.5×10^{39}	(6)
14–195	$< 3.0 \times 10^{42}$	This work

Extended Data Table 1 | Photometry of SBS 0335-052E. In the column of reference, (1), (2), (3), (4), (5), and (6) indicate ref.⁴⁵, ref.⁴⁶, ref.⁹, ref.⁴⁷, ref.⁴⁰, and ref.⁴, respectively. The optical fluxes are corrected for the Galactic extinction.

7. Reines, A. E., Johnson, K. E. & Hunt, L. K. a New View of the Super Star Clusters in the Low-Metallicity Galaxy SBS 0335-052. *Astron. J.* **136**, 1415–1426 (2008). 0807.1098.
8. Izotov, Y. I., Chaffee, F. H. & Schaerer, D. Deep spectroscopy of the low-metallicity blue compact dwarf galaxy SBS 0335-052. *Astron. Astrophys.* **378**, L45–L48 (2001). astro-ph/0109254.
9. Engelbracht, C. W. et al. Metallicity Effects on Dust Properties in Starbursting Galaxies. *Astrophys. J.* **678**, 804–827 (2008). 0801.1700.
10. Stern, D. et al. Mid-infrared Selection of Active Galactic Nuclei with the Wide-Field Infrared Survey Explorer. I. Characterizing WISE-selected Active Galactic Nuclei in COSMOS. *Astrophys. J.* **753**, 30 (2012). 1205.0811.
11. Jencson, J. E. et al. The SPIRITS Sample of Luminous Infrared Transients: Uncovering Hidden Supernovae and Dusty Stellar Outbursts in Nearby Galaxies. *Astrophys. J.* **886**, 40 (2019). 1901.00871.
12. Kokubo, M. et al. A Long-duration Luminous Type II In Supernova KISS15s: Strong Recombination Lines from the Inhomogeneous Ejecta-CSM Interaction Region and Hot Dust Emission from Newly Formed Dust. *Astrophys. J.* **872**, 135 (2019). 1901.05508.
13. Glass, I. S. Long-term infrared photometry of Seyferts. *Mon. Not. R. Astron. Soc.* **350**, 1049–1066 (2004). astro-ph/0402289.
14. Clavel, J., Wamsteker, W. & Glass, I. S. Hot Dust on the Outskirts of the Broad-Line Region in Fairall 9. *Astrophys. J.* **337**, 236 (1989).

15. Minezaki, T. et al. Inner Size of a Dust Torus in the Seyfert 1 Galaxy NGC 4151. Astrophys. J. Lett. **600**, L35–L38 (2004). [astro-ph/0311338](#).
16. Greene, J. E. & Ho, L. C. Estimating Black Hole Masses in Active Galaxies Using the H α Emission Line. Astrophys. J. **630**, 122–129 (2005). [astro-ph/0508335](#).
17. Yang, G. et al. X-CIGALE: Fitting AGN/galaxy SEDs from X-ray to infrared. Mon. Not. R. Astron. Soc. **491**, 740–757 (2020). [2001.08263](#).
18. González-Martín, O. et al. Hints on the Gradual Resizing of the Torus in AGNs through Decomposition of Spitzer/IRS Spectra. Astrophys. J. **841**, 37 (2017). [1704.06739](#).
19. Abramowicz, M. A., Chen, X., Kato, S., Lasota, J.-P. & Regev, O. Thermal Equilibria of Accretion Disks. Astrophys. J. Lett. **438**, L37 (1995). [astro-ph/9409018](#).
20. Abramowicz, M. A., Czerny, B., Lasota, J. P. & Szuszkiewicz, E. Slim Accretion Disks. Astrophys. J. **332**, 646 (1988).
21. Kehrig, C. et al. The extended He II λ 4686 emission in the extremely metal-poor galaxy SBS 0335 - 052E seen with MUSE. Mon. Not. R. Astron. Soc. **480**, 1081–1095 (2018). [1807.09307](#).
22. Reines, A. E. & Volonteri, M. Relations between Central Black Hole Mass and Total Galaxy Stellar Mass in the Local Universe. Astrophys. J. **813**, 82 (2015). [1508.06274](#).
23. Baldassare, V. F., Reines, A. E., Gallo, E. & Greene, J. E. A $\sim 50,000 M_{\odot}$ Solar Mass Black Hole in the Nucleus of RGG 118. Astrophys. J. Lett. **809**, L14 (2015). [1506.07531](#).

24. Thornton, C. E., Barth, A. J., Ho, L. C., Rutledge, R. E. & Greene, J. E. The Host Galaxy and Central Engine of the Dwarf Active Galactic Nucleus POX 52. *Astrophys. J.* **686**, 892–910 (2008). 0807.1535.
25. Übler, H. et al. A massive black hole in a low-metallicity AGN at $z \sim 5.55$ revealed by JWST/NIRSpec IFS. arXiv e-prints arXiv:2302.06647 (2023). 2302.06647.
26. Kocevski, D. D. et al. Hidden Little Monsters: Spectroscopic Identification of Low-Mass, Broad-Line AGN at $z > 5$ with CEERS. arXiv e-prints arXiv:2302.00012 (2023). 2302.00012.
27. Harikane, Y. et al. JWST/NIRSpec First Census of Broad-Line AGNs at $z=4-7$: Detection of 10 Faint AGNs with $M_{\text{BH}} \sim 10^6 - 10^7 M_{\text{sun}}$ and Their Host Galaxy Properties. arXiv e-prints arXiv:2303.11946 (2023). 2303.11946.
28. Planck Collaboration et al. Planck 2013 results. XVI. Cosmological parameters. *Astron. Astrophys.* **571**, A16 (2014). 1303.5076.
29. Wright, E. L. et al. The Wide-field Infrared Survey Explorer (WISE): Mission Description and Initial On-orbit Performance. *Astron. J.* **140**, 1868–1881 (2010). 1008.0031.
30. Mainzer, A. et al. Initial Performance of the NEOWISE Reactivation Mission. *Astrophys. J.* **792**, 30 (2014). 1406.6025.
31. Meisner, A. M., Caselden, D., Schlafly, E. F. & Kiwy, F. unTimely: a Full-sky, Time-domain unWISE Catalog. *Astron. J.* **165**, 36 (2023). 2209.14327.

32. Masci, F. J. & Fowler, J. W. AWAIC: A WISE Astronomical Image Co-adder. In Bohlender, D. A., Durand, D. & Dowler, P. (eds.) Astronomical Data Analysis Software and Systems XVIII, vol. 411 of Astronomical Society of the Pacific Conference Series, 67 (2009). 0812.4310.
33. Masci, F. ICORE: Image Co-addition with Optional Resolution Enhancement. Astrophysics Source Code Library, record ascl:1302.010 (2013). 1302.010.
34. Mizukoshi, S. et al. Measurement of AGN dust extinction based on the near-infrared flux variability of WISE data. Mon. Not. R. Astron. Soc. **516**, 2876–2886 (2022). 2209.07933.
35. Kelly, B. C. Some Aspects of Measurement Error in Linear Regression of Astronomical Data. Astrophys. J. **665**, 1489–1506 (2007). 0705.2774.
36. Fitzpatrick, E. L. Correcting for the Effects of Interstellar Extinction. Publ. Astron. Soc. Pac. **111**, 63–75 (1999). astro-ph/9809387.
37. Stalevski, M. et al. The dust covering factor in active galactic nuclei. Mon. Not. R. Astron. Soc. **458**, 2288–2302 (2016). 1602.06954.
38. Isobe, Y. et al. EMPRESS. IV. Extremely Metal-poor Galaxies Including Very Low-mass Primordial Systems with $M_* = 10^4\text{-}10^5 M_\odot$ and 2%-3% (O/H): High (Fe/O) Suggestive of Metal Enrichment by Hypernovae/Pair-instability Supernovae. Astrophys. J. **925**, 111 (2022). 2108.03850.
39. Virtanen, P. et al. SciPy 1.0: fundamental algorithms for scientific computing in Python. Nature Methods **17**, 261–272 (2020). 1907.10121.

40. Hunt, L. K. et al. ALMA observations of cool dust in a low-metallicity starburst, SBS 0335-052. Astron. Astrophys. **561**, A49 (2014). 1312.0944.
41. Oh, K. et al. The 105-Month Swift-BAT All-sky Hard X-Ray Survey. Astrophys. J. Suppl. Ser. **235**, 4 (2018). 1801.01882.
42. Yang, G. et al. Fitting AGN/Galaxy X-Ray-to-radio SEDs with CIGALE and Improvement of the Code. Astrophys. J. **927**, 192 (2022). 2201.03718.
43. Just, D. W. et al. The X-Ray Properties of the Most Luminous Quasars from the Sloan Digital Sky Survey. Astrophys. J. **665**, 1004–1022 (2007). 0705.3059.
44. Morrison, R. & McCammon, D. Interstellar photoelectric absorption cross sections, 0.03-10 keV. Astrophys. J. **270**, 119–122 (1983).
45. Papaderos, P., Izotov, Y. I., Fricke, K. J., Thuan, T. X. & Guseva, N. G. On the age of the nearby blue compact dwarf galaxy SBS 0335-052. Astron. Astrophys. **338**, 43–55 (1998).
46. Vanzì, L., Hunt, L. K., Thuan, T. X. & Izotov, Y. I. The near-infrared view of SBS 0335-052. Astron. Astrophys. **363**, 493–506 (2000). astro-ph/0009218.
47. Dale, D. A. et al. Multiwavelength Observations of the Low-Metallicity Blue Compact Dwarf Galaxy SBS 0335-052. Astron. J. **122**, 1736–1746 (2001). astro-ph/0107108.
48. Bruzual, G. & Charlot, S. Stellar population synthesis at the resolution of 2003. Mon. Not. R. Astron. Soc. **344**, 1000–1028 (2003). astro-ph/0309134.

49. Boquien, M. et al. CIGALE: a python Code Investigating GALaxy Emission. Astron. Astrophys. **622**, A103 (2019). 1811.03094.
50. Dale, D. A. et al. A Two-parameter Model for the Infrared/Submillimeter/Radio Spectral Energy Distributions of Galaxies and Active Galactic Nuclei. Astrophys. J. **784**, 83 (2014). 1402.1495.
51. Stalevski, M., Fritz, J., Baes, M., Nakos, T. & Popović, L. Č. 3D radiative transfer modelling of the dusty tori around active galactic nuclei as a clumpy two-phase medium. Mon. Not. R. Astron. Soc. **420**, 2756–2772 (2012). 1109.1286.

H α Line Component	Flux [erg s $^{-1}$ cm $^{-2}$]	FWHM [km s $^{-1}$]
Narrow	$1.81 (\pm 0.007) \times 10^{-13}$	$1.58 (\pm 0.001) \times 10^2$
Medium	$2.40 (\pm 0.02) \times 10^{-15}$	$1.29 (\pm 0.01) \times 10^3$
Broad	$4.80 (\pm 0.04) \times 10^{-15}$	$1.24 (\pm 0.01) \times 10^4$

Extended Data Table 2 | Fluxes and line widths for the three components of the H α emission.

Parameter	Value
Star formation history (<code>sfhdelayed</code> module)	
e -folding time of the main stellar population, <code>tau_main</code> (Myr)	1, 10 , 100
age of the main stellar population, <code>age_main</code> (Myr)	100
Single stellar population (<code>bc03</code> module; ref. ⁴⁸)	
Metallicity	0.0001 , 0.0004
Dust attenuation (<code>dustatt_powerlaw</code> module; ref. ⁴⁹)	
<code>Av_young</code>	0.01, 0.03, 0.05 , 0.1
<code>uv_bump_amplitude</code>	0.0, 0.75
Galactic dust emission (<code>dale2014</code> module; ref. ⁵⁰)	
AGN emission (<code>skirtor2016</code> module; ref. ^{37,51})	
Average edge-on optical depth at 9.7 micron	7,9, 11
Index that sets dust density gradient with polar angle	1.5
Ratio of outer to inner torus radius	10
Inclination angle i	0, 10, 20, 30, 40, 50, 60, 70, 80, 90
AGN fraction in total IR luminosity	0.1, 0.3, 0.7, 0.8, 0.9, 0.95
$E(B - V)$ of polar dust	0.05, 0.1
Polar dust temperature	100, 200 , 300

Extended Data Table 3 | CIGALE parameter ranges used for the SED fitting. The best-fit values of the parameters are shown in bold. Parameter ranges that are not specified in this table are set to the default values of CIGALE.